Surface & Coatings Technology 202 (2008) 5804–5811

Contents lists available at ScienceDirect

Surface & Coatings Technology

journal homepage: www.elsevier.com/locate/surfcoat

Phase formation in a Ni–50Cr HVOF coating

J. Saaedi [a,b,*], T.W. Coyle [a], S. Mirdamadi [b], H. Arabi [b], J. Mostaghimi [a]

[a] *Centre for Advanced Coating Technologies, Department of Materials Science and Engineering, University of Toronto, Toronto, Canada*
[b] *Department of Materials and Metallurgical Engineering, Iran University of Science and Technology, Tehran, Iran*

ARTICLE INFO

Article history:
Received 24 December 2007
Accepted in revised form 27 May 2008
Available online 13 June 2008

Keywords:
HVOF
Thermal-spray coatings
Ni–50Cr
Non-equilibrium phases
Sigma phase

ABSTRACT

A complex, fine scale microstructure of non-equilibrium phases is obtained by HVOF deposition of Ni–50Cr alloy due to the rapid cooling experienced by the splats which make up the as-deposited coatings. XRD analyses indicated that the as-deposited coatings consisted predominantly of a single fcc γ-Ni phase. Two small peaks suggested the presence of NiO and/or $NiCr_2O_4$ at the limit of detection (~5%). Shoulders on the main γ-Ni peaks were interpreted as evidence of a second, lower Cr content γ-Ni phase. Characterization of the oxide content of the as-deposited coatings by X-ray diffraction, image analysis of backscattered electron images, and electron probe microanalysis yielded conflicting results due to the size of the microstructural features present relative to the spatial resolution of these techniques. Due to the nature and feature size of the non-equilibrium oxide phase(s), direct measurement of the oxygen content by EPMA was found to be the most accurate technique. Heat treatment of an as-deposited coating at 650 °C in vacuum resulted in coarsening of the microstructural features, and an approach towards a mixture of equilibrium phases consisting of γ-Ni, α-Cr, and Cr_2O_3. Evidence was also seen in the XRD pattern of an intermetallic σ phase that has previously only been reported in thin films of Ni–Cr alloys.

1. Introduction

Nickel–chromium alloys attract the attention of metal scientists by their high temperature corrosion properties [1]. The presence of chromium in the alloys results in formation of an oxide layer which reduces further oxidation and hot corrosion. Alloys with 43 wt.% chromium or less tended to display discontinuous oxide formation and local spalling [2] when exposed to type I hot corrosion conditions (molten ash environment containing sodium sulfate and/or potassium sulfate at temperatures ranging from 850 to 950 °C). Alloys with higher chromium content tended to display thinner, more continuous surface oxides and less hot corrosion penetration into the alloy. On the other hand, nickel alloys containing more than 30% chromium are extremely difficult to fabricate by conventional hot working processes because of the development of a brittle alpha chromium phase. Once α-Cr is present, the alloy is more difficult to work because α-Cr is hard to deform and less ductile than γ-Ni. In addition, high-chromium nickel-based alloys are susceptible to a decrease in ductility after exposure to elevated service temperatures [2].

In recent years there has been a growing interest in the use of high velocity oxy-fuel (HVOF) thermal spraying for depositing protective coatings of various materials on a wide variety of substrates [3–5]. Coatings deposited by other thermal-spray processes had limited usefulness as corrosion protection coatings due to the presence of interconnected porosity in the structure. However, HVOF coatings can be produced with less porosity than other types of thermal-sprayed coatings and are now extensively studied for their corrosion-resistant properties [6].

Co-extruded INCOCLAD 671 / 800H tubing (a corrosion-resistant 50Ni–50Cr alloy clad on an alloy 800H core) has been used successfully in the heat-exchanger sections of coal-fired utility boilers since the early 1970's [7,8]. Furthermore, positive experience was reported on the use of 50%Cr–50%Ni as a metal dusting resistant coating [9]. An HVOF sprayed 50Ni–50Cr coating yielded good protection until 750 °C in ultra-supercritical (USC) boiler components [10].

The development of corrosion and erosion protective coatings using thermal-spray techniques requires in-depth knowledge of the principal characteristics of these products [11]. The heated and potentially molten, oxidized, or vaporized particles strike the substrate whereupon they deform (i.e., "splat") and adhere through predominantly mechanical mechanisms [12]. Because the splat is rapidly quenched upon impact, the deposit may consist of an amorphous, microcrystalline, or fine-grained mixture of both thermodynamically meta-stable and stable phases [13].

The purpose of the present communication is to describe the complex microstructure of phases obtained by HVOF spraying of Ni–50Cr alloy, and to discuss the limitations of standard characterization techniques in analyzing such microstructures. To date, only a small number of studies have been reported in the open literature focused on

---

[*] Corresponding author. Present address: 8th Floor, Bahen Building, 40 St. George Street, Toronto, Ontario, Canada M5S 3G8. Tel.: +1 416 635 5309; fax: +1 416 946 8252.
E-mail address: jahan.saaedi@utoronto.ca (J. Saaedi).

0257-8972/$ – see front matter © 2008 Elsevier B.V. All rights reserved.
doi:10.1016/j.surfcoat.2008.05.056

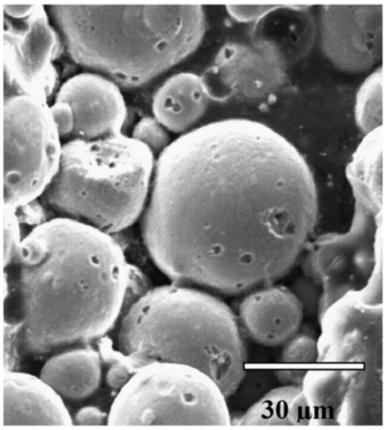

Fig. 1. SE image of AMDRY 350F powder.

the characterization of the microstructure and phase composition of HVOF sprayed coatings of Ni–50Cr and similar alloys. Most studies of coatings of this alloy have dealt with the evaluation of the performance of the coatings when exposed to environments typical of practical service conditions.

2. Experimental methods

The coatings were deposited by means of a Sulzer Metco DJ 2700 Diamond Jet Gun onto stainless steel plates to a thickness of approximately 200 µm. Nitrogen was selected as the carrier gas and the fuel gas was propylene. Online diagnostic measurements were carried out using the Tecnar DPV-2000 diagnostic system to measure particle characteristics in-flight and better understand the deposit formation.

Powder particle size was determined using a Malvern Mastersizer particle size analyzer. Cross-sections of the powder particles were prepared by mounting the particles in resin and then grinding and polishing. Coated substrates were sectioned and polished for microstructural characterization using optical microscopy and scanning electron microscopy (SEM). Energy dispersive X-ray spectroscopy (EDS) analyses were performed during SEM examination. The scanning electron microscopes used in this work were a JEOL JSM-840 (SEM) complemented by a PGT/AAT EDS detector (thin window), and a Hitachi S-4500 field emission (FE-SEM) instrument.

The phase compositions of the powder and coatings were characterized by X-ray diffraction (XRD) using a Philips PW 2273/20 diffractometer with Cu K_α radiation and a scanning rate of 1.45° 2θ/min. The diffractometer was operated at 40 kV and 40 mA. The XRD analyses were conducted on a lightly compacted powder sample and the top as-deposited surface of the coatings. The lattice parameters of the powder and coatings were determined by calculating the lattice parameter from the three most intense fcc peaks in the XRD patterns, plotting these against $\cos^2\theta/\sin\theta$, and extrapolating the line of best fit to $\theta=0$ to eliminate the effect of displacement error [14].

Line scans and semi-bulk elemental analyses on cross-sections of coatings were carried out by electron probe microanalysis (EPMA, Cameca SX50) using a Ni alloy (NIST certificate, SRM 1244–NiCr, 73Ni16Cr10Fe), Cr_2O_3, and NiO as standards. Spectra were recorded at 1 µm intervals during the line scans. The semi-bulk analyses were carried out by collecting spectra from 10 to 12 non-overlapping 40 µm × 60 µm square areas on the coating cross section of each sample.

Clemex image analysis software was utilized in order to quantify the porosity level and oxide content in the coatings. Images for image analysis were obtained from as-polished surfaces using light microscopy, or secondary electron (SE) or backscattered electron (BSE) signals in the SEM. Heat treatments were carried out on coated samples at 650 °C for 1 and 4 h under vacuum (10^{-5} mb) in a Red Devil high temperature vacuum furnace.

3. Results and discussion

3.1. Ni–50Cr powder

Commercial Ni–50Cr powder from the Sulzer Metco Company (AMDRY 350F) was used for the study. The nominal composition of the alloy was Cr-49.6% C-0.03% Fe-0.1% Mn-0.1% Si-0.3% Ni-balance (in wt.%). A secondary electron image of the powder particles is shown in Fig. 1. The majority of the particles have a near-spherical morphology, typical of powder produced by inert gas atomization. The particle size distribution is shown in Fig. 2. The median particle size was 35 µm; 25 vol.% was smaller than 20 µm.

3.2. HVOF spraying

A set of eight experiments with five variable factors was designed for the initial stage of process optimization. Oxygen flow, fuel flow, air flow, standoff distance, and feed rate were considered as the main controllable factors of the spray process. Particle velocity and particle temperature at the substrate position were selected as measurable outcomes. Table 1 summarizes the two most promising combinations of processing parameters, which were used to deposit the coatings characterized in this study. Among the eight experiments, the conditions used for Coating 2 produced the highest particle velocity along with a relatively low particle temperature. The fuel/oxygen ratio for Coating 2 was 0.28, which is fuel-rich and about 1.3 times the stoichiometric ratio of 0.22. The fuel/oxygen ratio was 0.17 (fuel-lean condition) for Coating 1, for which the particles had a lower velocity and lower temperature in-flight. However the difference in particle temperatures may be placed on the range of DPV standard error.

3.3. Optical microscopy

Optical micrographs of as-polished cross-sections of coatings are shown in Figs. 3 and 4. The coatings were extremely dense and the splats were wide and flat. The porosity levels of Coatings 1 and 2 were less than 1%, as measured by image analysis. In addition to the light contrast matrix of coating alloy, there were darker areas which occupied an extensive part of the microstructures. Some of these areas were very dark with a contrast close to that of the pores. More unmelted particles can be seen in Coating 1, suggesting lower particle temperatures during the spraying process.

3.4. X-ray diffraction

The diffraction pattern of the powder exhibited three peaks which could be assigned to the (111), (200) and (220) planes of γ-Ni. This

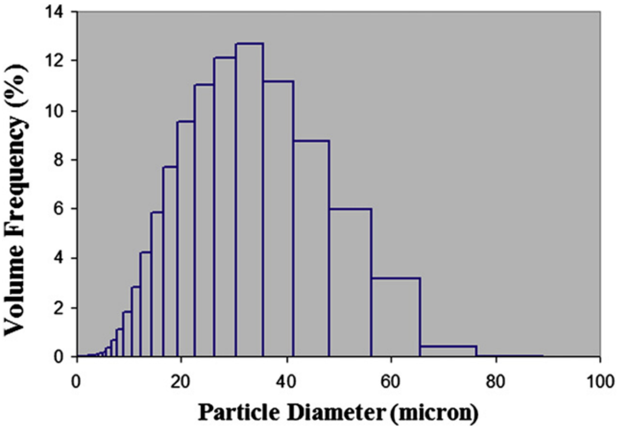

Fig. 2. Particle size distribution of used commercial powder particles.

Table 1
Parameter settings for the samples examined

Parameter Coating	Oxygen flow (SLM)	Fuel flow (SLM)	Air flow (SLM)	Carrier gas flow (SLM)	Stand-off distance (mm)	Feed rate (g/min)	Transverse gun speed (mm/s)	Particle temperature (°C)	Particle velocity (m/s)
1	350	60	405	9	200	23	170	2188±165	599±85
2	300	85	355	9	200	23	170	2196±204	646±148

indicated that the powder was in a supersaturated meta-stable state with a lattice parameter of 0.3611 nm (Fig. 5). This is significantly larger than the lattice parameter of pure Ni which is 0.3524 nm [15]. The existence of a single phase structure in this powder has been pointed out previously [16,17].

For the HVOF coatings similar patterns with minor differences were obtained. The lattice parameter of γ-Ni for Coating 1 and Coating 2 were determined to be 0.3609 and 0.3604 nm, respectively. This indicates that the composition of the γ-Ni phase in the coatings has not changed significantly compared to that of the powder. The main peak of the α-bcc chromium phase, which is an equilibrium phase constituent in this alloy, would appear at 44.37° [19] and so may contribute to the broadening of the major γ-Ni peak. However, shoulders were also observed on the high 2θ side of the 2nd and 3rd highest γ-Ni peaks. The shoulders on all three γ-Ni peaks may be due to the presence of a second γ-Ni phase with lower chromium content due to evaporation of Cr species from the surface of the particles in-flight or taking Cr in adjacent oxide phase, as discussed further below. The formation of the α-bcc chromium phase from the supersaturated γ-Ni phase was likely inhibited by the rapid cooling experienced by both the powder particles and the splats.

Two additional small, broad peaks could be seen in the XRD patterns of the coatings (especially in Coating 1). These broad peaks were located near the positions of major peaks of nickel and nickel chromium oxides, although it was not possible to unambiguously attribute them to a known crystalline phase. The presence of these oxides could be related to the very short oxidation time during the HVOF process, typically less than 0.01 s [21]. It has been reported that Ni-containing oxides grow much more rapidly than chromium oxide; the formation of NiO and $NiCr_2O_4$ before Cr_2O_3 may be an example of a transient oxidation phenomenon [22].

The coating samples were heat treated at 650 °C under vacuum to attempt to develop the weakly diffracting phases suggested to be present in the XRD patterns of the as-deposited coatings. This is higher than the temperature (300 °C) at which the crystallization of chromium oxide from an amorphous mixed oxide was reported to occur [23], and also above the temperature in which the equilibrium two-phase mixture of bcc α-Cr and fcc γ-Ni forms (500°–600 °C) [24]. The XRD patterns of samples heat treated for 1 and 4 h were nearly identical. They exhibited sharp peaks which could be assigned to four different phases: fcc γ-Ni with a lattice parameter of 0.3569 nm, bcc α-Cr, Cr_2O_3, and Cr_7Ni_3, an intermetallic sigma phase. The XRD pattern of the sample heat treated for 4 h is shown in Fig. 6.

The first result to be noted in the XRD patterns of heat treated samples was the formation of a significant amount of crystalline Cr_2O_3. The transient phases disappeared and were also turned into Cr_2O_3. The amount of Cr_2O_3 present after heat treatment is qualitatively in accord with the total oxygen content measured by EPMA (see below) in the as-deposited coatings. The increase in bulk oxygen content during heat treatment was negligible compared with the oxygen content of the as-deposited coatings, which suggests that the Cr_2O_3 formed from weakly diffracting non-equilibrium oxide phases, amorphous or poorly crystallized mixed oxides, and oxygen trapped in splat boundaries or other pores in the as-deposited coatings.

The second significant change in the pattern was the disappearance of the shoulders on the high 2θ side of the of the 2nd and 3rd highest γ-Ni peaks, coinciding with the development of stronger α-Cr peaks. This supports the suggestion that the shoulders on the γ-Ni peaks in the patterns of the as-deposited coatings were due to the presence of a second, lower Cr content fcc γ-Ni phase. The shift of the main γ-Ni peaks to higher 2θ positions may represent the equilibration of the Cr content within a single γ-Ni phase.

Another important result is the formation of a sigma phase in the coating after a relatively short time (1 h) at an intermediate temperature (650 °C). The sigma phase is commonly found in Fe–Cr alloys. In the Ni–Cr phase diagram, a σ phase is predicted at about 70 at.% Cr below 600 °C, but it has not yet been observed in bulk alloys [24]. The σ phase has been found in Ni–Cr thin films [27,28]. Yukawa et al. [27] determined the lattice parameters of the tetragonal σ phase to be $a=0.881$ nm and $c=0.457$ nm. The lattice parameters calculated from the International Center for Diffraction Data (ICDD) reference pattern [26] are $a=0.869$ nm and $c=0.450$. The ICDD report noted that the σ phase appeared along with a "small amount of Cr_2O_3." In the present work, $a=0.865$ nm and

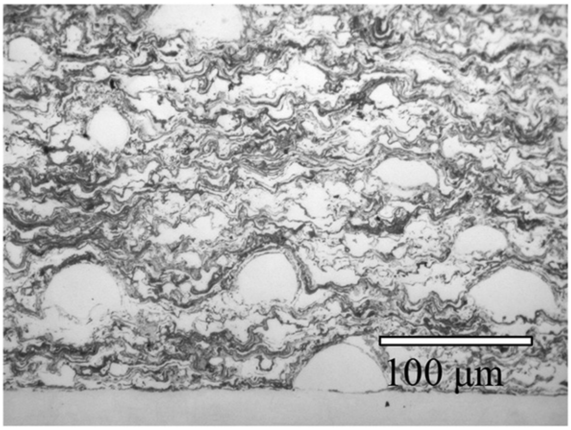

Fig. 3. Light microscope image of the as-polished Coating 1.

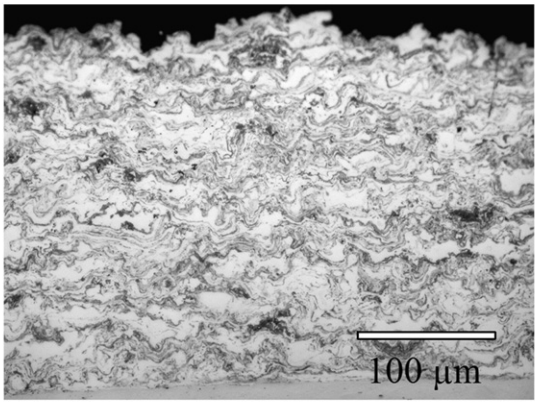

Fig. 4. Light microscope image of the as-polished Coating 2.

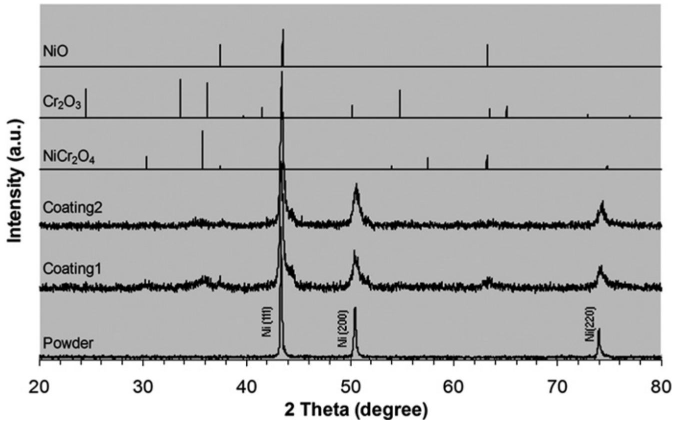

Fig. 5. XRD patterns of the powder and coatings in comparison to the reference patterns of $NiCr_2O_4$ [18], Cr_2O_3 [19], and NiO [20].

c = 0.449 nm for the 1 h heat treatment and a = 0.870 nm and c = 0.451 nm for the 4 h heat treatment. The composition of the σ phase observed here appears to approach a steady state composition (lattice parameter) with increased heat treatment time.

3.5. Scanning electron microscopy

3.5.1. SEM imaging

In SEM images formed by backscattered electrons (BSE), the contrast is related to the atomic number of the elements present; phases containing lower atomic number elements, like oxides, appear darker. The various constituents of thermal-spray coatings (oxide, porosity and matrix phase) can generally be identified and selected by means of their differences in grey contrast under BSE imaging conditions. In BSE images of the coatings deposited in this study several levels of contrast were evident.

A typical BSE image of the microstructure of Coating 2 is shown in Fig. 7a. It consists of the following areas (indicated by arrows in Fig. 7a): 1) the light grey contrast matrix, 2) medium grey contrast (MGC) areas, 3) dark grey contrast (DGC) areas, 4) a very low content of porosity which appears black, and 5) a white phase. The microstructure of Coating 1 exhibited the same combination of features and contrasts under BSE imaging as Coating 2.

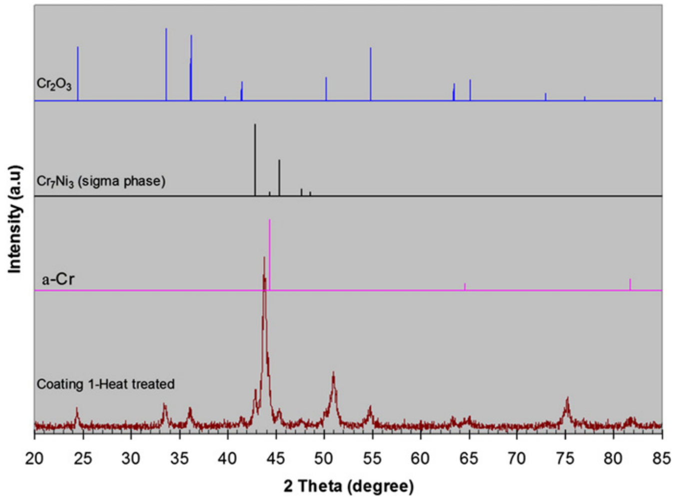

Fig. 6. XRD pattern of heat treated Coating 1 after a 4 h heat treatment in comparison to the reference patterns of α-Cr [25], Cr_7Ni_3 [26], and Cr_2O_3 [19].

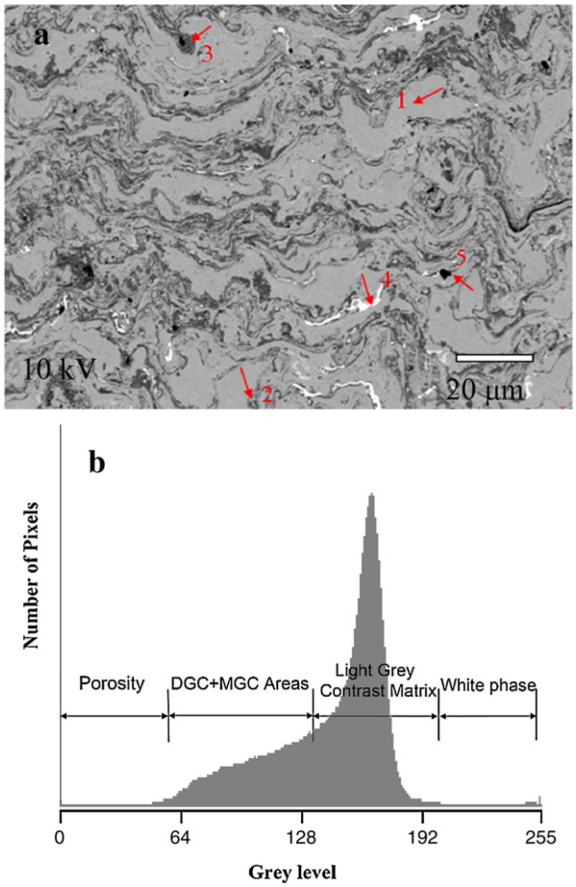

Fig. 7. (a) BSE–SEM image of the Coating 2 and (b) the histogram of pixel grey levels corresponding to the image shown in (a). The ranges of pixel intensities assigned to the various phases in the micrograph are indicated in (b).

The grey level of each pixel in a digital image is used in image analysis to differentiate between features of interest within an image. As can be seen in the histogram of pixel grey levels shown in Fig. 7(b), the black to DGC area transition and light grey (matrix) to white transition are reasonably well defined, however there were no sharp cutoffs or obvious discontinuities within the range of grey level corresponding to the MGC and DGC areas. This range of grey level is generally associated with oxide phases in the microstructure, therefore setting grey level thresholds during image analysis in order to determine oxide content was difficult. The area fraction occupied by the MGC and DGC areas was on the order of 0.30 to 0.40 for the two coatings, depending on the position of the threshold. This would correspond to $NiCr_2O_4$ weight fractions of 0.22 to 0.31, much higher than the amount of oxide that would have been expected based on the XRD patterns for the as-deposited coatings. The white phase is related to contamination of the Ni–50Cr powder by tungsten-bearing powder particles, and will not be addressed further in this report.

Higher magnification images obtained with the FE-SEM from Coating 2 are shown in Fig. 8a, b and c. The MGC and DGC areas consist of submicron scale features which were not discernable in the lower magnification images. DGC, MGC, and light grey areas are intimately intertwined at a scale at or below the resolution limit of the backscattered images. The broad intermediate grey level range observed in these micrographs appears, therefore, to be related to the size of the microstructural features relative to the resolution of the SEM images.

The resolution is limited by the nature of the electron-beam–specimen interaction [29, p 178–179] which determines the volume of material from which the electrons used to form the SEM image are collected. The dimension of the signal-producing area contains

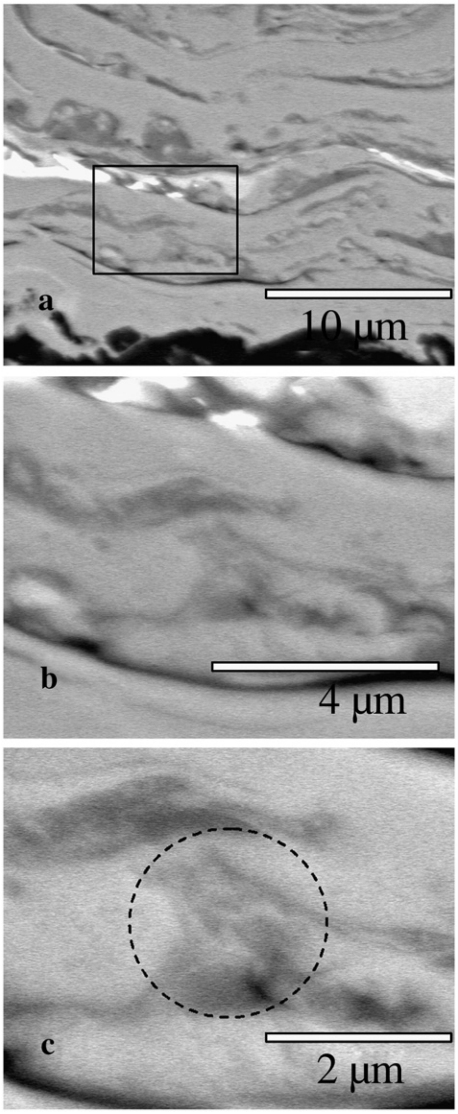

Fig. 8. FE-SEM backscattered electron images of Coating 2.

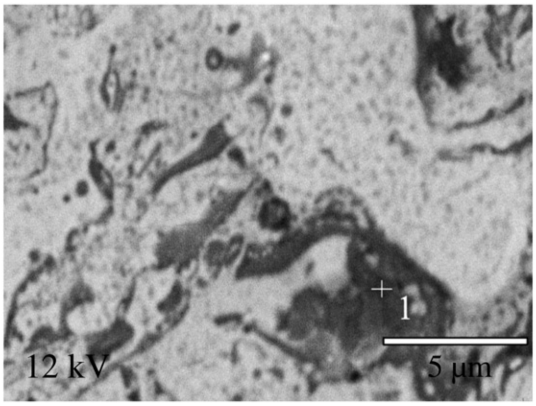

Fig. 10. BSE image of the Coating 2 after heat treatment at the same magnification.

contributions from the finite size of the beam as well as the projected surface area of backscatter emission due to electron scattering. The diameter of the effective signal-producing area is found by adding in quadrature the beam diameter d_{B} and the diameter of the signal-producing area d_{BSE}: $d_{\mathrm{eff}} = \sqrt{d_{\mathrm{B}}^2 + d_{\mathrm{BSE}}^2}$ [30, p 162]. Assuming d_{BSE} to be a fraction of the Kanaya–Okayama range, $d_{\mathrm{BSE}} = 0.3R_{\mathrm{KO}}$ [29, p 121], the diameter of the effective signal-producing area for an accelerating voltage of 20 kV is found to be 0.5, 0.7, and 1 µm for Ni–50Cr, NiO, and Cr_2O_3, respectively. Since R_{KO} depends primarily on the accelerating voltage, the resolution in BSE imaging can be improved by reducing the interaction volume by operating at lower accelerating voltages. For an accelerating voltage of 10 kV, the signal-producing area for Ni–50Cr alloy, NiO, and Cr_2O_3, is 0.17, 0.2, and 0.3 µm respectively. The beam diameter in a conventional SEM operated under conditions providing good BSE imaging contrast is on the order of 50 to 100 nm. In field emission imaging, the beam size is on the order of 5 nm or less. In neither case would the beam diameter be a significant contributor to the overall spread of the BSE signal.

The area circled in Fig. 8(c) would have been considered to be an MGC area in low magnification images, but in fact appears to consist of a mixture of light grey γ-Ni matrix and DGC oxide phases. The size of the γ-Ni and oxide features are smaller than the effective signal-producing area for backscattered electron imaging under these conditions. Thus, the boundaries between these phases do not show a sharp transition in contrast, but rather a fuzzy boundary with a range of intermediate grey levels is seen. Therefore, the ability of image analysis to accurately determine the fraction of oxide phases in these samples is affected.

BSE images of Coating 2 in as-deposited condition and after the 4 h heat treatment are shown in Figs. 9–12. No significant differences compared to the corresponding as-deposited coating could be seen at magnifications lower than 1000×. At higher magnifications, a new phase could be seen homogeneously distributed throughout the γ-Ni phase, Fig. 10. The new phase was identified as the equilibrium bcc α-Cr phase

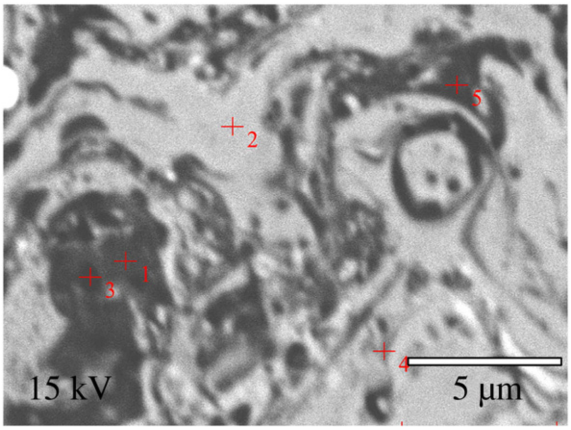

Fig. 9. BSE image of Coating 2 before heat treatment.

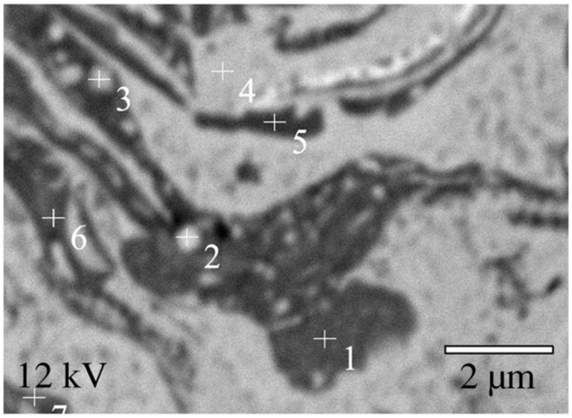

Fig. 11. BSE image of the heat treated Coating 2 after etching.

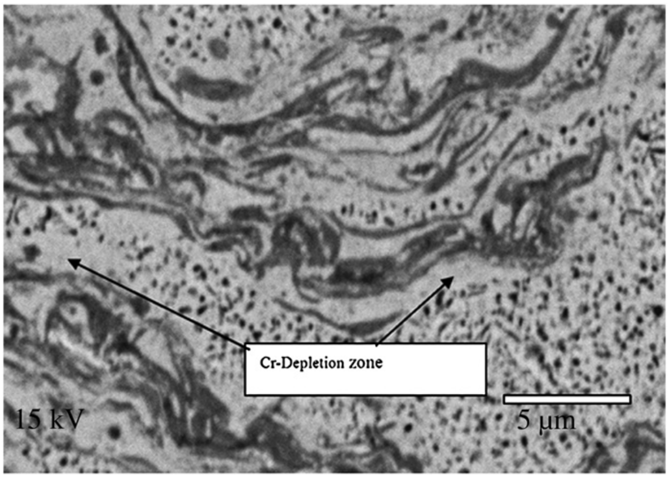

Fig. 12. BSE image of the heat treated Coating 2 after etching illustrates Cr depletion zones.

observed in the XRD patterns of the heat treated coating. The features previously described as MGC and DGC areas were still present.

In an attempt to identify where in the microstructure the σ phase detected in the XRD patterns of heat treated samples was located, polished sections were etched with aqua regia [31]. Unfortunately the σ phase could not be identified, however two microstructural features were more clearly evident after etching. The fine features within the MGC areas had coarsened during heat treatment such that they became visible at intermediate magnifications, Fig. 11. In addition, Cr depleted zones could be seen adjacent to the DGC areas, as shown in Fig. 12. The phenomenon of chromium depletion due to selective oxidation is well known for bulk Ni–50Cr alloy [22]. Here the depletion zone becomes apparent after heat treatment due to the lack of α-Cr precipitates in these areas. Apparently the Cr content in these regions did not exceed the solubility limit of Cr in the γ-Ni.

The depletion zones likely formed during the spraying process and are responsible for the shoulders seen on the high 2θ side of the main γ-Ni peaks in the XRD patterns of the as-deposited coatings. However it may be possible that depletion zone continued to form during heat treatment along with Cr_2O_3 precipitation. Heat treatment of the coatings leads to formation of α-Cr particles in the interior of the supersaturated γ-Ni splats, but not in the low chromium content depletion zone. Therefore, after heat treatment the chromium content within the γ-Ni phase was uniform, the main γ-Ni peaks in the XRD patterns of heat treated coatings shifted to slightly higher 2θ positions, and the shoulders on those peaks disappeared.

3.5.2. EDS-SEM analysis

Energy dispersive X-ray spectroscopy (EDS) spot analyses in the areas indicated by arrows 1 (light grey matrix) and 2 (MGC) in Fig. 7a showed that the Ni/Cr ratios were approximately the same in these areas (Fig. 13a and b). This ratio was somewhat lower in dark grey contrast areas (arrow 3 in Fig. 7a) which indicated a higher concentration of the lighter element, i.e. chromium (Fig. 13c). In general the EDS spot analyses performed on these areas did not show a significant difference in the Ni/Cr ratio among the various contrast areas, although the oxygen concentration increased as the contrast became darker (compare the height of the oxygen peaks in Fig. 13a, b, and c). As was the case for image analysis based on contrast differences in BSE images, the very fine scale features of this microstructure complicate the compositional analysis of the coatings due to the limited spatial resolution of EDS. The performed EDS analyses on numbered areas of Figs. 9–11 were not leaded to new results.

The volume of material from which X-ray signals are generated due to the impinging electrons may be estimated from an equation developed by Anderson and Hasler which describes the X-ray generation range (R_x) as a function of energy loss and density of the matrix [32, p 83]. The estimate for Ni alloys with an electron accelerating voltage of 20 kV would $R_x \approx 0.8$ μm, and $R_x \approx 0.2$ μm for 12 kV. The lower density of the oxide phase would lead to a larger X-ray generation range: $R_x \approx 1.2$ μm for a 12 kV accelerating voltage. The spatial resolution of EDS analyses depends on the radius of the area from which signal is collected ($\sim R_x$) and the probe size [32, p 83]. As was the case for the resolution of BSE images, the probe size is generally much smaller than the X-ray generation range, and therefore the spatial resolution is approximately equal to R_x.

Given the submicron size of the microstructural features with the DGC and MGC areas (Fig. 8c), the EDS results presented in Fig. 13 represent averaged compositions of the phases within the X-ray generation range. To improve spatial resolution lower accelerating voltages were used during the analysis of heat treated samples. The Ni/Cr ratio in DGC and MGC areas was lower when a 12 kV accelerating voltage was used, but the resolution was still insufficient to identify the Cr_2O_3 phase shown to exist in heat treated samples by XRD. Since the minimum electron energy required to excite the K_α X-ray emission from Ni is approximately 7.478 keV, the 12 kV accelerating voltage represents a practical lower limit.

Elemental maps were produced using long EDS pulse-processing times to obtain a better sense of the distribution of oxygen, Cr, and Ni in the microstructure (Fig. 14). The relatively long accumulation time of 4500 s for each element was chosen to detect constituents present at low concentrations or which produced low count rates, never-the-less the detection limit was ~5 wt.% [30, p 534]. The oxygen and Cr concentrations in the DGC and MGC areas were clearly higher, and Ni concentrations lower, than the background, but nickel and chromium concentration differences corresponding to the depletion zones were not distinguishable.

3.6. Electron probe X-ray microanalysis

To obtain quantitative analyses of the oxygen content in the coatings, EPMA was conducted on Coating 1 and Coating 2. The analyses were performed at 15 kV and 23 nA. The corresponding probe size for this current may be estimated as 0.1 μm using the probe diameter-vs-probe

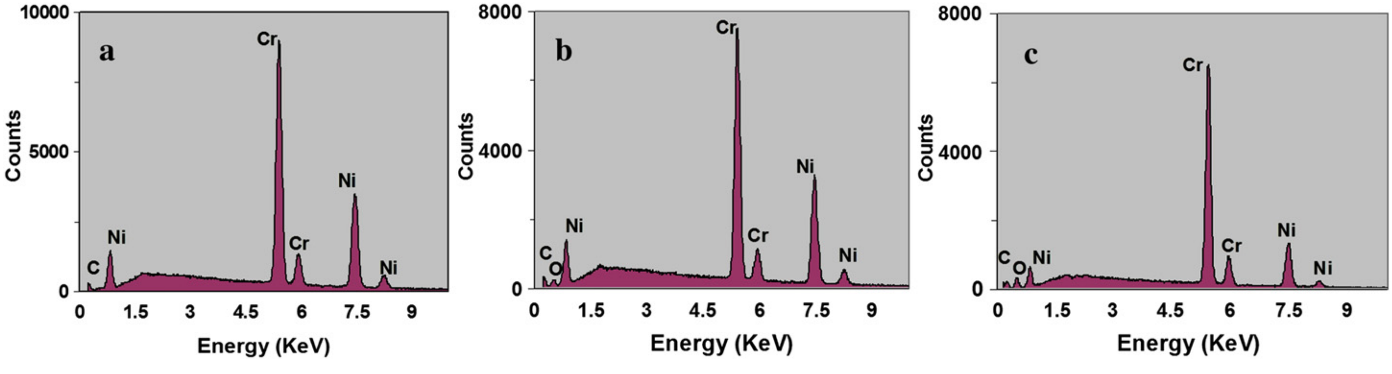

Fig. 13. EDS spot analyses at an accelerating voltage of 20 kV of areas indicated by (a) arrow 1 (light grey matrix), (b) arrow 2 (MGC) and (c) arrow 3 (DGC) in Fig. 7a.

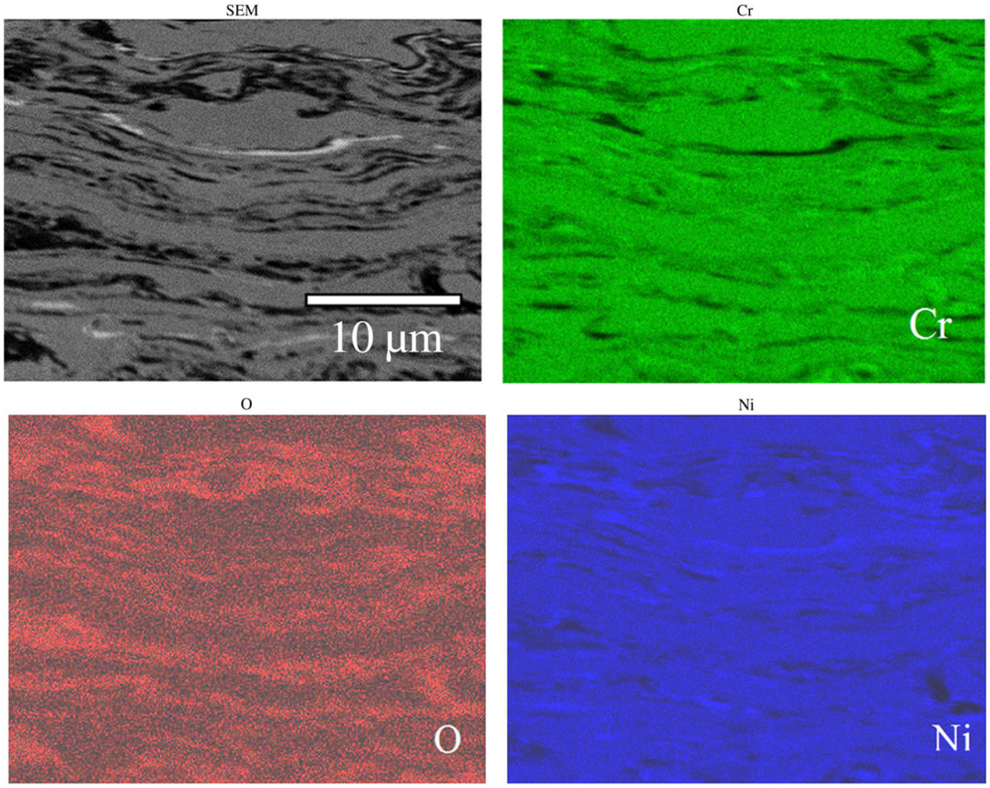

Fig. 14. EDS elemental maps of Cr, O, and Ni in Coating 2.

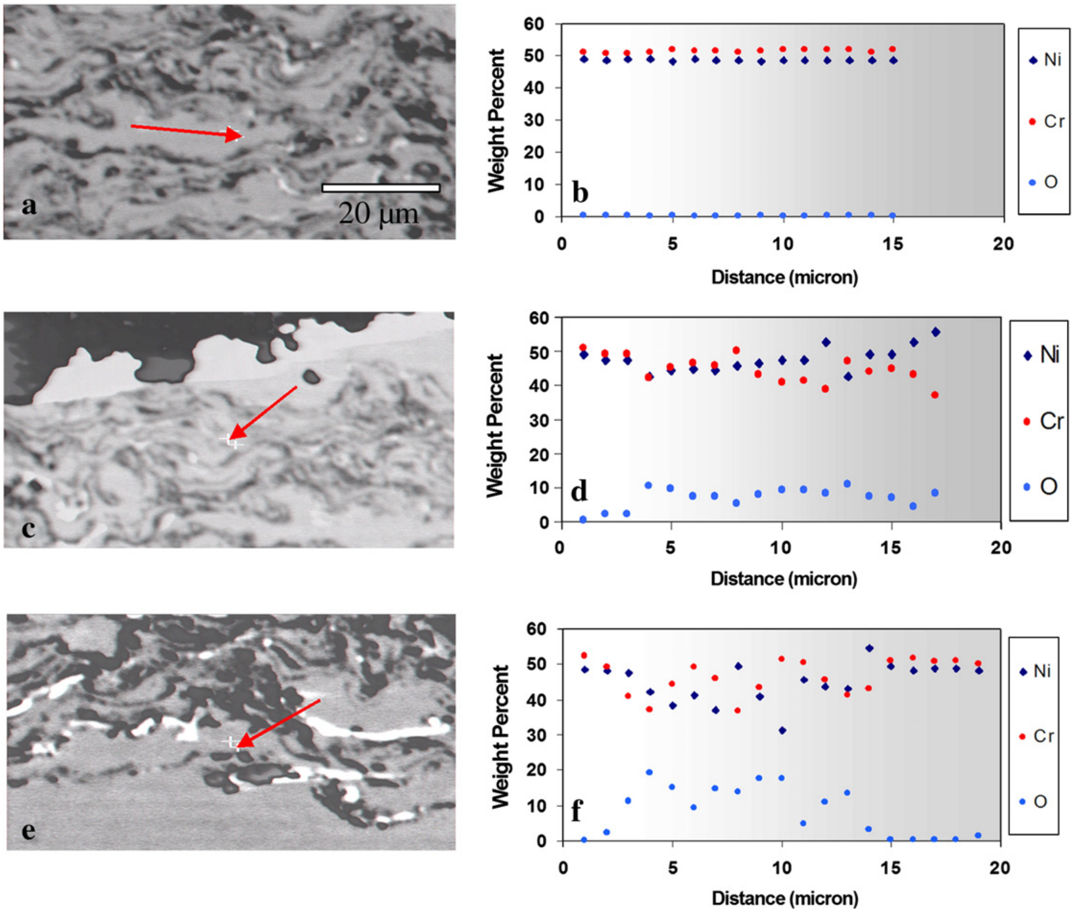

Fig. 15. EPMA line scans and corresponding images of three different areas of Coating 2, (a) and (b) through an un-melted particle, (c) and (d) through an area mostly included medium gray contrasts, (e) and (f) through an area mostly included dark grey contrasts.

current curves [29, p 46]. The X-ray spatial resolution (the sum of R_x and the probe size) was ~0.6 µm.

The average oxygen contents of Coating 1 and Coating 2, obtained by averaging the results collected from at least ten 40 µm by 60 µm windows, were 7.04 and 6.79 wt.%, respectively. This indicated that these different process conditions have not had much effect on oxide level of coatings. The standard deviations were 0.85 and 0.99 respectively which could mainly be contributed to oxygen (oxide) inhomogeneity in cross section of the coatings. Some oxygen may exist as gas phase trapped within splat boundaries or other pores. If the total measured oxygen is assumed to be present as $NiCr_2O_4$, the average oxide contents of Coating 1 and Coating 2 would be 24.9 wt.% and 24.0 wt.%, respectively. The average oxide contents of the Coating 1 and Coating 2 would be 22.3 wt.% and 21.5 wt.% if Cr_2O_3 was assumed to be the only existing oxide present in the coatings. These estimates are at the lower limit of the range obtained by image analysis.

Elemental line scan analyses were conducted through three different areas of Coating 2, as shown in Fig. 15. The results in each graph are related to the quantitative contents of Ni, Cr and O elements. Line scan 1 passed through a semi–melted particle, to allow comparison with the initial powder composition. The Ni and Cr contents were 48–49 and 51–52 wt.% respectively (Fig. 15b). The nominal composition of the initial powder was 49.9% Ni and 49.6% Cr, therefore no significant change in the Ni:Cr ratio is evident. The oxygen content in the center of the particle ranged from 0.1 to 0.2 wt.%. Line scan 2 passed through a mainly MGC area and line scan 3 through a mainly DGC area. The oxygen content in the MGC area ranged from ~5 to ~10 wt.% (Fig. 15d), and from ~9 to ~19 wt.% in the DGC area (Fig. 15f). Since the solubility of oxygen in pure chromium and nickel is low, normally less than 0.1% [33], the oxygen quantities measured by EPMA analyses of MGC and DGC areas must be related to the presence of oxide compounds. As discussed previously, NiO, Cr_2O_3 and $NiCr_2O_4$ are the most probable oxide compounds; their oxygen contents are 21.42, 31.58, and 28.23 wt.%, respectively. As was the case for the EDS analyses, these quantitative results and the fluctuations in composition seen in the graphs of the EPMA line scans, are consistent with mixtures of oxide and metallic phases at a scale below the spatial resolution of the EPMA technique.

The Cr migration from matrix into oxide phases could have a detrimental effect on the coating properties. Corrosion properties of coatings decrease when alloys lose their original chemistry, including oxides of important elements, Cr and Ni. Residual stresses are a difficult problem in oxidized coatings, because the fracture strength and ductility of the coatings have decreased. Thermal and electrical conductivity in oxidized bulk materials decrease as well, and therefore it is expected that oxidized coatings will not be an exception.

4. Summary and conclusions

1– Dense coatings of Ni–50Cr with less than 1% porosity and high oxide content were deposited by HVOF spraying using fuel to oxygen ratios of 0.77 and 1.32 times of the stoichiometric ratio. With these deviations around the stoichiometric ratio, it was found that there are no significant differences between deposited coatings with respect of porosity level and oxide content.

2– The as-deposited microstructures of HVOF Ni–50Cr have been found to consist of high and low Cr γ-Ni metallic regions along with NiO and/or $NiCr_2O_4$ oxides. The oxides were weakly diffracting to X-rays, suggesting that they were poorly crystallized or existed as very thin layers or small particles.

3– XRD underestimated the amount of oxide present at the limit of detection (~5%). EPMA measurements indicated an average oxygen content of 7.04 wt.% for Coating 1 and 6.79 wt.% for Coating 2, which would correspond to 24.9 and 24.0 wt.% $NiCr_2O_4$. Image analysis overestimated the oxide weight fractions in the range 0.22–0.31 since only a fraction of the DGC and MGC areas consisted of oxide phases. The oxide phases transformed to well crystallized Cr_2O_3 after heat treatment at 650 °C under vacuum and their fraction was in line with expectations based on the EPMA measurement of oxygen in the as-deposited coating.

4– The broad, continuous range of grey contrast levels obtained within areas of the microstructures contributing to oxide phases indeed were a mixture of metallic and oxide phases with features sized less than 0.5 µm and being below the spatial resolution limit for EPMA and EDS analyses. The nature of these non-equilibrium oxide phases requires further study.

5– Heat treatment at 650 °C in vacuum resulted in coarsening of the microstructural features, and an approach toward an equilibrium phase composition consisting of Cr_2O_3, γ-Ni, and α-Cr. This occurred as the result of precipitation of particles of α-Cr uniformly throughout the γ-Ni matrix, except in a thin zone along the splat boundaries consistent with depletion of Cr in that zone to form oxides. Evidence was also seen in the XRD pattern of an intermetallic phase (sigma phase) that has previously only been reported in thin films of Ni–Cr alloys.

6– Given the limitations of image analysis and XRD in accurately determining the oxide content of as-deposited coatings of this alloy, the bulk oxygen content should be measured directly. EPMA analysis conducted over large areas is a convenient way to do this, since separation of the coating from the substrate is not required.

Acknowledgments

Thanks are expressed to Dr. Larry Pershin for help with deposition of the coatings and George Kretschmann for valuable discussions and help with the SEM imaging, EDS and X-ray diffraction analyses. Partial support for J. Saaedi during the course of this work was provided by the Centre for Advanced Coating Technologies, University of Toronto, Toronto, Canada, Professor Javad Mostaghimi, Director.

References

[1] V.P. Kolotushkin, V.P. Kondrat'ev, Met. Sci. Heat Treat 45 (11–12) (2003) 411.
[2] D.A. Shifler and L.K. Kohler, CORROSION/2000 NACE, Houston 2000, Paper No. 00242.
[3] H. Edris, D.G. McCartney, A.J. Sturgeon, J. Mater. Sci. 32 (1997) 863.
[4] D.W. Parker, G.L. Kutner, Adv. Mater. Proc. 4 (1991) 68.
[5] J. Stokes, L. Looney, Surf. Coat. Technol. 148 (1) (November 1 2001) 18.
[6] T.S. Sidhu, S. Prakash, R.D. Agrawal, Mater. Sci. 41 (6) (2005).
[7] P. Ganesan, C.S. Tassen, J. Mater. Eng. 10 (3) (1988) 171.
[8] M.G. Fahrmann and G.D. Smith, CORROSION/2000 NACE, Houston 2000, Paper No. 00232.
[9] H.L. Holland, CORROSION/2001 NACE, Houston 2001, Paper No. 01385.
[10] T. Sundararajan, S. Kuroda, F. Abe, Metall. Mater. Trans. A 35A (Oct. 2004) 3187.
[11] V. Higuera, F.J. Belzunce, A. Carriles, S. Poveda, J. Mater Sci 37 (2002) 649.
[12] K. Luer, J. Du Pent, A. Marder, CORROSION/1999 NACE, Houston 1999, Paper No. 298.
[13] R.C. Tucker, J. Vac. Sci. & Tech. 11 (4) (July/Aug. 1974) 725.
[14] B.D. Cullity and S.R. Stock, Elements of X-ray Diffraction, Third edition, Prentice Hall, 2001, p 363.
[15] JCPDS, International Centre for Diffraction Data, 1998, PDF # 00-004-850.
[16] T. Sundararajan, S. Kuroda, K. Nishida, T. Itagaki, F. Abe, Iron and Steel Institute of Japan (ISIJ) 44 (2004) 139.
[17] T. Sundararajan, S. Kuroda, T. Itagaki, F. Abe, Iron and Steel Institute of Japan 43 (1) (2003) 104.
[18] JCPDS, International Centre for Diffraction Data, 2005, PDF # 01-075-1728.
[19] JCPDS, International Centre for Diffraction Data, 2005, PDF # 01-070-3765.
[20] JCPDS, International Centre for Diffraction Data, 2005, PDF # 00-001-1239.
[21] K. Korpiola, "High temperature oxidation of metals, alloy and cermet powders in HVOF spraying process", Doctoral Thesis, Helsinki University of Technology, 2004.
[22] N. Birk, G.H. Meier, Introduction to High Temperature Oxidation of Metals, First edition, Edward Arnold Publishers, Ltd, 1983, p. 107.
[23] Z. Yingjie, Q. Yitai, Z. Manwei, Mater. Sci. Eng. B41 (1996) 294.
[24] W. Bruckner, W. Pitschke, J. Thomas, J. Appl. Phys. 87 (5) (2000).
[25] JCPDS, International Centre for Diffraction Data, 2004, PDF # 01-089-4055.
[26] JCPDS, International Centre for Diffraction Data, 2005, PDF # 00-051-0637.
[27] N. Yukawa, M. Hida, T. Imura, M. Kawamura, Y. Mizuno, Metall. Trans 3 (1972) 887.
[28] M.B. Vollaro, D.I. Potter, Thin Solid Films 239 (1994) 37.
[29] J. Goldstein, D.E. Newbury, P. Echlin, D. Joy, C. Fiori, E. Lifshin, Scanning Electron Microscopy and X-ray Microanalysis, First edition, Plenum Press, 1981.
[30] J. Goldstein, D.E. Newbury, P. Echlin, D. Joy, A. Roming, C. Lyman, C. Fiori, E. Lifshin, Scanning Electron Microscopy and X-ray Microanalysis, 2nd edition, Plenum Press, 1992.
[31] G.F. Vander Voort, Metallography, Principles and Practice, McGraw-Hill, 1984, p. 649.
[32] J. Goldstein, H. Yakowitz, Practical Scanning Electron Microscopy, Plenum Press, 1975.
[33] J.E. Croll, G.R. Wallwork, Oxid. Met. 1 (1) (1969).